This article may be downloaded for personal use only. Any other use requires prior permission of the author and AIP Publishing. This article appeared in Zun-Di Huang, Cheng Peng, Zheng-Wei Chen, Zi-Jian Guo, Ning Chang, Hong-Bei Chen, Wei-Kai Kong, You-Biao Wang; Compressible effects of a supersonic evacuated tube maglev train at various Mach numbers. Physics of Fluids 1 December 2024; 36 (12): 126126 and may be found at https://doi.org/10.1063/5.0247678.

RESEARCH ARTICLE | DECEMBER 11 2024

Compressible effects of a supersonic evacuated tube maglev train at various Mach numbers

Special Collection: Flow and Civil Structures

Zun-Di Huang (黄尊地); Cheng Peng (彭程) ; Zheng-Wei Chen (陈争卫) ; Zi-Jian Guo (郭子健); Ning Chang (常宁); Hong-Bei Chen (陈鸿倍); Wei-Kai Kong (孔维锴); You-Biao Wang (王友彪)

Check for updates

Physics of Fluids 36, 126126 (2024)
https://doi.org/10.1063/5.0247678

View Online Export Citation

Articles You May Be Interested In

Aerodynamic and shock wave investigation in hyperloop: Comparative analysis of maglev support configurations

Physics of Fluids (March 2025)

Dynamic transition of flow field for accelerating and decelerating process of evacuated tube train

Physics of Fluids (March 2025)

Aerodynamic phenomena and drag of a maglev train running dynamically in a vacuum tube

Physics of Fluids (September 2022)

09 January 2026 03:26:12

Physics of Fluids

AIP Publishing

AIP Publishing

Physics of Fluids

Special Topics Open for Submissions

Learn More

Physics of Fluids ARTICLE pubs.aip.org/aip/pof

Compressible effects of a supersonic evacuated tube maglev train at various Mach numbers

Cite as: Phys. Fluids **36**, 126126 (2024); doi: 10.1063/5.0247678
Submitted: 8 November 2024 · Accepted: 22 November 2024 ·
Published Online: 11 December 2024

View Online Export Citation CrossMark

Zun-Di Huang (黄尊地),[1] Cheng Peng (彭程),[2] Zheng-Wei Chen (陈争卫),[3,a)] Zi-Jian Guo (郭子健),[3] Ning Chang (常宁),[1] Hong-Bei Chen (陈鸿倍),[1] Wei-Kai Kong (孔维锴),[1] and You-Biao Wang (王友彪)[4]

AFFILIATIONS

[1]School of Rail Transportation, Wuyi University, Jiangmen 529000, China
[2]School of Mechanical and Automation Engineering, Wuyi University, Jiangmen 529000, China
[3]Department of Civil and Environmental Engineering, The Hong Kong Polytechnic University, Hong Kong, China
[4]Railway Science & Technology Research & Development Center, China Academy of Railway Sciences Corporation Limited, Beijing 100081, China

Note: This paper is part of the special topic, Flow and Civil Structures.
[a)]**Author to whom correspondence should be addressed:** zhengwei.chen@polyu.edu.hk

ABSTRACT

Evacuated tube maglev train (ETMT) system aims to advance ultra-high-speed transportation, featuring unique high-speed flow phenomena and complex shockwave dynamics in low-pressure environments that demand further exploration. This paper examines the flow structures and aerodynamic loads of the ETMT over a range of Mach numbers from 0.8 to 2.0. Leveraging a compressible, density-based solver based on the Advection Upstream Splitting Method, extensive numerical simulations of the ETMT were conducted across transonic and supersonic regimes, revealing diverse aerodynamic characteristics under varying operational conditions. The research delineates how aerodynamic properties distinctively shift with operating Mach numbers. In supersonic conditions, distinct shockwave effects emerge prominently, and as the train's velocity escalates, there is a consistent reduction in overall drag and lift coefficients, resulting in a net reduction of 32% in the total train drag coefficient (a most economical Mach number of 1.8) and the lift diminished by 38%. However, notable disparities exist in the drag and lift coefficients among different train sections. These insights are instrumental in understanding the aerodynamic behavior of tube trains at ultra-high speeds and serve as a crucial guide for the train's exterior design.

Published under an exclusive license by AIP Publishing. https://doi.org/10.1063/5.0247678

09 January 2026 03:26:12

I. INTRODUCTION

Magnetic levitation trains, renowned for their swift speeds, minimal vibration, and low noise levels, have emerged as a cornerstone in the evolution of rail transport.[1,2] In a visionary quest for next-generation, highly efficient transportation systems, a novel integration of evacuated tube transport with superhigh-speed maglev trains has been advanced.[3] This innovative approach brings maglev train technology to the threshold of sonic speeds and beyond. Recently, the concept of evacuated tube maglev train (ETMT) has increasingly gripped the public imagination, tracing back to Robert Goddard's seminal 1904 proposal and further elaborated in the 1930s by Herman Kemper in his patent applications for maglev trains.[4,5] Despite protracted research and intermittent advancements due to various societal factors, the project's evolution presses forward. In 2013, Elon Musk coined the term "Hyperloop" for this avant-garde tube transport system.[4] By 2017, Hyperloop One had erected the globe's first test track for superhigh-speed rail, clocking speeds up to 387 km/h. In the same vein, Virgin Hyperloop conducted its inaugural manned trial, propelling its high-speed levitation transport system to 172 km/h within 6.25 s. In China, the world's first test platform for high-temperature superconducting maglev vehicles named "Super-Maglev" has been pioneered.[6] Prominent nations such as Germany, Japan, and China are spearheading the rapid development of maglev systems. Technology's promise of high efficiency, energy conservation, lighter structures, reduced pollution, and minimal noise heralds a revolutionary leap in rail technology. Leading projects like the long-anticipated Swiss metro and the contemporary Hyperloop initiatives underscore this strategic direction. Continued research is penetrating deeper into the fundamental and technical aspects of ETMT.

As the surrounding air reaches sufficient density, the impact of resistance on vehicle dynamics becomes significant, underscoring the necessity for meticulous aerodynamic considerations.[7–11] The flow

Published under an exclusive license by AIP Publishing

dynamics induced by the Evacuated Tube Maglev Train (ETMT) involves one or more trains operating within a tube, generating forward compressive and rearward expansive disturbances, collectively defined as tube train flow.[12] The low-pressure environment is also pivotal in augmenting the levitation capabilities of the ETMT. This flow scenario involves the rapid relative motion between the tube walls and the train, characterized by intricate internal and external flow dynamics.[13] The high velocities initiate profound aerodynamic disturbances, extending the flow's longitudinal dimension considerably. These disturbances travel substantially further within the tube before dissipating, setting tube train flow apart from conventional open-air or tunnel-based train travel.[14,15] With the increase in vacuum degrees, the expansion area of the train's wake contracts and the strength of shock waves are mitigated, contributing to the improved stability of the train within the tube.[16] This distinctiveness necessitates focused research.

In-depth investigations by numerous scholars into the fundamental scientific issues related to vacuum tube maglev transportation have led to notable advancements in computational fluid dynamics (CFD) in the ETMT arena.[14,17–22] To alleviate choking effects and enhance operational efficiency, optimizing the design of the train's exterior[23,24] and the tube structure[25,26] remains a fervent focus of contemporary research. The operation of supersonic trains within sealed tubes has unveiled novel aerodynamic phenomena.[27–29] It is particularly notable that when the ETMT operates, pressure resistance is more pronounced than shear resistance.[30,31] To significantly reduce the aerodynamic drag and energy consumption of the train, it is crucial to refine the train's frontal design and the tube's structural configuration.[32] Moreover, during deceleration, pressure drag exceeds that experienced during acceleration,[33] and the aerodynamic performance of a multi-vehicle ETMT system demonstrates that decreased inter-vehicle spacing markedly reduces aerodynamic drag, with this effect being more pronounced at elevated Mach numbers.[33] Zhou *et al.*[28] and Zhou and Zhang[34] have detailed the emergence and evolution of wave phenomena—specifically shockwaves and expansion waves—highlighting the occurrence of normal shockwaves, reflected shockwaves, and expansion waves within the tube. The phenomenon of aerodynamic heating, due to the train's operation in an enclosed tube, is significant. Temperatures within the tube are predominantly influenced by pressure waves, with the foremost areas of the train experiencing the highest temperatures, primarily attributed to normal shockwaves.[28,34] The interplay of shock and expansion waves leads to relatively cooler temperatures at the train's rear,[34] and there exists an approximate linear relationship between the blockage ratio and the tube wall temperatures.[35] Moreover, the initial ambient temperature inside the tube also affects the flow structure of the train's wake.[36] Additionally, the interaction and reflection of shock and expansion waves on the tube walls, a result of tube effects, can induce vibrations in the tube structure.[27,30,37]

Research to date has largely focused on the aerodynamic drag impacts during low to medium speed operations of maglev train at subsonic velocities below 600 km/h.[38,39] Notably, when the Mach number falls below 0.65, both the total and pressure drag coefficients initially rise with increases in train speed and subsequently diminish as the speed decreases.[40] In contrast, the shear drag coefficient follows an opposing trend.[31,41] Investigations into the aerodynamic characteristics of trains operating at supersonic speeds in environments with pressures below ambient atmospheric levels remain exceedingly rare. Furthermore, most numerical studies have relied on simplistic two-dimensional, axisymmetric models of trains and tubes, which fail to account for ground effects and track configurations.[17,20] The narrow suspension gaps inherent in these models can significantly influence the formation of wave systems, while the compressible flows at ultra-high speeds give rise to a plethora of nonlinear phenomena.[42] Therefore, this paper introduces a comprehensive three-dimensional ETMT model that incorporates rail for better analyzing aerodynamic characteristics across a range of Mach numbers in both transonic and supersonic conditions. Section II details the computational models for both the tube and train, including the methods used for setting up CFD simulations. Section III discusses the validation of the CFD models, incorporating both grid independence tests and wind tunnel experiment verifications. Section IV offers a detailed analysis of the data collected. This paper concludes with Sec. V, summarizing the key findings and implications.

II. METHODOLOGY

A. Geometric model and boundary condition

This research utilizes a maglev train model, as illustrated in Figs. 1(a) and 1(b) as the geometric model. The train's height, $H = 4.2$ m, is used as the characteristic length to dimensionally scale other measurements. The width of the train is $0.88H$, and its total length is $L = 19.04H$, segmented into the head carriage, middle carriage, and tail carriage, each, respectively, measuring $6.42H$, $6.20H$, and $6.42H$. The tube model, inspired by high-speed rail tunnel architectures, is depicted as a straight tube; simplifications were made to the track model to ease mesh generation around the track area. The cross-sectional area of the train is 11.91 m^2, that of the tunnel is 49 m^2, and the track's cross-sectional area is 1.84 m^2, which results in an operational blockage ratio for the train of 0.253. A 1/10 scaled model was utilized in the simulations. To rigorously examine the impact of the train's operating speed on its aerodynamic characteristics, this study designs a spectrum of operational scenarios, extensively detailed in

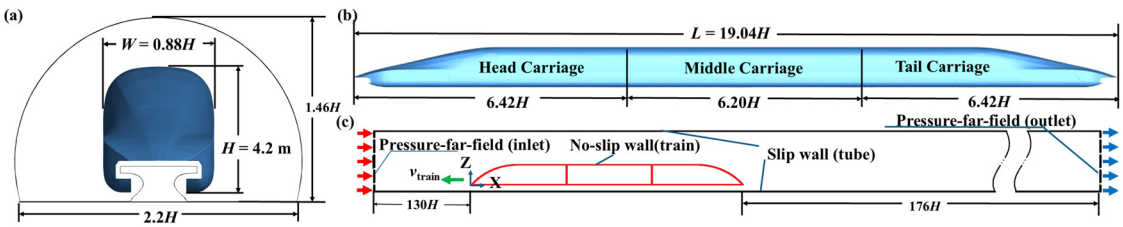

FIG. 1. Geometric model and boundary conditions: (a) the front view of both the train and tube, (b) the side dimensions of the train, and (c) computational domain and boundary conditions.

09 January 2026 03:26:12

Published under an exclusive license by AIP Publishing

TABLE I. Parameter variables across different operating conditions.

Condition	*Ma*	$v_{tr}/(km \cdot h^{-1})$	Vacuum (atm)	Blockage ratio
Case-1	0.80	979.2		
Case-2	1.00	1224.0		
Case-3	1.20	1468.8		
Case-4	1.40	1713.6	0.1	0.253
Case-5	1.60	1958.4		
Case-6	1.80	2203.2		
Case-7	2.00	2448.0		

Table I of the document. These scenarios contain various train speeds and corresponding environmental setups to enable a comprehensive comparative analysis.

The tube train operates within a narrowly elongated tube, allowing for the disregard of boundary disturbances at both ends. This study concentrates on dissecting the aerodynamic characteristics around the tube train, significantly curtailing the computational domain's length using a non-reflective pressure-far-field approach. As depicted in Fig. 1(c), in alignment with the train's velocity and the computational domain requirements of railway tube,[20,43] the diameters at both ends of the tube are established at 130 and 176 times the tube train's characteristic length, respectively. The pressure-far field, apt for compressible flow models with infinite free-stream conditions, sets the domain's inlet and outlet to accommodate inflow under pressure-far-field conditions and eliminating the Riemann reflection, specifying incoming Mach number, temperature, and pressure. The train's surface features a no-slip stationary wall, while the tube walls are treated with a slip condition, synchronous with the inflow's velocity. An environmental pressure of $p_0 = 0.1$ atm and an initial temperature of $T_0 = 298.15$ K (25 °C) are maintained.

B. Meshing strategy

The volumetric mesh utilizes a trimmer-hexahedral topology in STAR-CCM+. This mesh configuration incorporates prism layers at the boundary surfaces to enhance detail and accuracy. In the broader mesh areas, a pristine hexahedral mesh is constructed and seamlessly connected to the outer mesh through a process of strategic cutting or "trimming" of the outer hexahedral structures, which integrate these with the prism layers.[44] Given the significant variations in the flow field around the train, the mesh is meticulously refined in the areas immediately preceding and following the train to enhance accuracy in simulations.[45,46] As shown in Figs. 2(a) and 2(f), multi-level refinement zones are strategically employed to enhance the resolution of flow solutions in critical areas, including the wake region, underneath the train, and along the tracks. Twenty-two layers of prism mesh are assembled on the train and the tube, with a stretch ratio of 1.1 to resolve the viscous sublayer within the turbulent boundary layer, as depicted in Figs. 2(b)–2(e). The thickness of the first prism layer is set at 0.2 mm to achieve a y^+ value of 1.

C. Data preprocessing

To ensure the accuracy and comparability of the results, the data dimensionless has been rendered. Here are the definitions for the aerodynamic drag coefficient (C_d), lift coefficient (C_l), pressure coefficient (C_p), and temperature ratio (C_T),

$$C_p = \frac{p - p_0}{0.5\rho {v_{tr}}^2}, \tag{1}$$

$$C_d = \frac{F_d}{0.5\rho A_{tr} {v_{tr}}^2}, \tag{2}$$

$$C_l = \frac{F_l}{0.5\rho A_{tr} {v_{tr}}^2}, \tag{3}$$

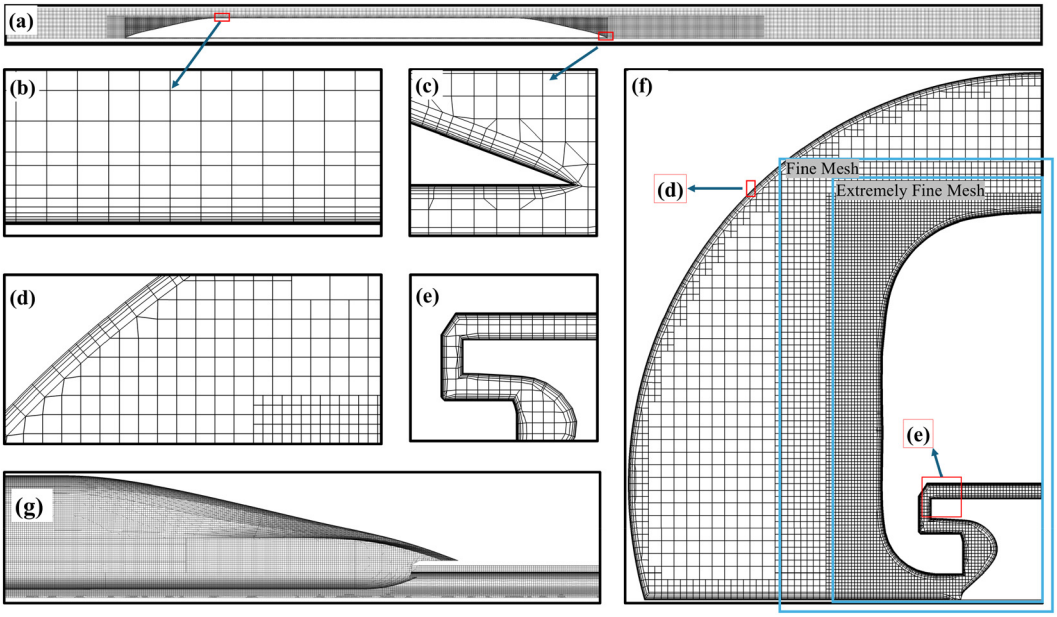

FIG. 2. The Mesh of the tube and the train: (a) the longitudinal section, (g) the surface mesh, (f) the cross section, and (b)–(e) the boundary layers.

09 January 2026 03:26:12

Published under an exclusive license by AIP Publishing

$$C_T = \frac{T - T_0}{T_0}, \tag{4}$$

where F_d and F_l represent aerodynamic drag and lift, respectively, while p and T denote absolute pressure and temperature, respectively. These variables are computed using fluid dynamics software. Assuming a constant gas temperature and molar mass, the air density ρ correlates directly with environmental pressure; hence at 0.1 atm, it is set to 1.225×10^{-1} kg/m^3. The train's velocity v_{tr} is calculated as $v_{tr} = Ma{\cdot}c$, where $c = 340$ m/s represents the speed of sound. The train's cross-sectional area $A_{tr} = 11.91$ m^2 reflects the maglev's largest x-directional projection. The standard ambient temperature T_0 is maintained at 298.15 K.

The overall drag (F_d) comprises pressure-induced drag (F_{dp}) and friction-induced drag (F_{df}), defined as

$$C_{dp} = \frac{F_{dp}}{0.5\rho A_{tr} {v_{tr}}^2}, \tag{5}$$

$$C_{df} = \frac{F_{df}}{0.5\rho A_{tr} {v_{tr}}^2}, \tag{6}$$

where C_{dp} and C_{df} represent the pressure and friction drag coefficients, respectively, cumulatively defined as C_d.

D. Numerical configuration

For the presented investigation into the aerodynamic effects of the ETMT, several foundational assumptions will be established: (1) The train operates at its top speed in a straight trajectory with uniform velocity, overlooking the phases of acceleration and deceleration; (2) Both the tube and the train's skin are modeled as sealed, smooth, adiabatic surfaces, discounting any external or internal heat transfer; (3) The air within the tube is evenly mixed, and the temperature and pressure are homogeneously distributed before the train's motion commences; (4) The internal air is considered as a calorically perfect gas whose specific heat capacity remains stable regardless of temperature or pressure variations. Given the high-speed movement of the train within a closed tube, the study had to accommodate the air's compressibility by applying three-dimensional, transient, and compressible flow equations. These equations account for air density and dynamic viscosity in accordance with the ideal gas law and Sutherland's law.[23,47]

The Improved Delayed Detached Eddy Simulation (IDDES) was employed for turbulence modeling. For complex flows such as flow separation and reattachment, the IDDES method can more accurately predict flow characteristics and is suitable for flows with complex boundaries and geometrical shapes.[48] This method, an advancement over the standard Detached Eddy Simulation (DES), combines the Reynolds-Averaged Navier–Stokes (RANS) model for boundary layers and irrotational flows with Large Eddy Simulation (LES) for the remaining flow areas. IDDES enhances DES by integrating wall-modeled LES, which significantly optimizes the balance between computational precision and processing time. This approach has become a staple in the aerodynamics analysis of trains due to its efficacy.[49–51] Facing rigorous simulation demands, a dual-stage simulation protocol was adopted to quickly stabilize convergence: initial steady-state simulations using the shear stress transport (SST) k-ω RANS model followed by transient analyses with the SST k-ω IDDES model, both implemented using the Advection Upstream Splitting Method. This methodology not only stabilizes the flow field but also captures essential physical data at constant-speed conditions and dynamic phenomena such as choked flow and shockwaves, with a convergence threshold for residuals set at 1×10^{-6}.

The tube's airflow was deemed compressible and treated with a viscous model based on Sutherland's law, solved using an implicit, density-based solver. Spatial discretization was managed via a least squares gradient method, enhancing cell-center calculations, while turbulence and dissipation terms were discretely handled using a second-order upwind approach to maximize accuracy. The transient simulations provided detailed insights into specific aerodynamic phenomena such as choked flow and shockwaves. Due to varied intake Mach numbers and evolving flow dynamics, achieving a stable state required different durations for each design scenario, with total simulation times consistently exceeding 1.5 s.

III. VERIFICATIONS

A. Mesh independent validation

To effectively utilize computational resources while ensuring accuracy, the presented study defined three mesh configurations:[52] Coarse mesh, Middle mesh, and Fine mesh. Each was assessed under a condition of $Ma = 1.8$ to compare aerodynamic drag and lift coefficients as outlined in Eqs. (2) and (3) from Sec. II D. According to Table II, discrepancies in drag coefficients across the meshes were minimal, yet lift coefficients showed greater variability. The relative error between Middle and Fine meshes was less than 5%, while it surpassed 5% between Coarse and Fine meshes, indicating that the Middle mesh strikes an optimal balance between precision and resource usage.

The distribution of pressure and temperature coefficients along the $Y = 0$ plane is presented at Fig. 3, which reveals consistent trends in pressure and temperature coefficients across the mesh settings, confirming that primary flow characteristics are well captured even by the Coarse mesh. However, detailed comparisons highlight notable discrepancies in pressure and temperature around the train's mid and rear sections when using the Coarse mesh, while the Middle and Fine meshes demonstrate closer agreement. Thus, the Middle mesh sufficiently resolves essential flow features without incurring additional computational costs and time.

B. Numerical verifications

Numerical methodologies are required to precisely simulate intricate flow dynamics, necessitating the implementation of wind tunnel experiments and the application of Computational Fluid Dynamics (CFD) to replicate these phenomena and confirm the reliability of CFD setup methodologies. However, as the evacuated tube maglev train (ETMT) remains in the developmental phase, wind tunnel experiments are infrequently conducted, particularly under supersonic

TABLE II. C_d and C_l of the maglev train under different mesh configurations.

Items	Coarse mesh	Middle mesh	Fine mesh
Grid amount (million)	10.56	21.15	33.24
C_d	1.625	1.709	1.746
Relative error	6.93%	2.14%	···
C_l	0.543	0.520	0.497
Relative error	9.35%	4.42%	···

09 January 2026 03:26:12

Published under an exclusive license by AIP Publishing

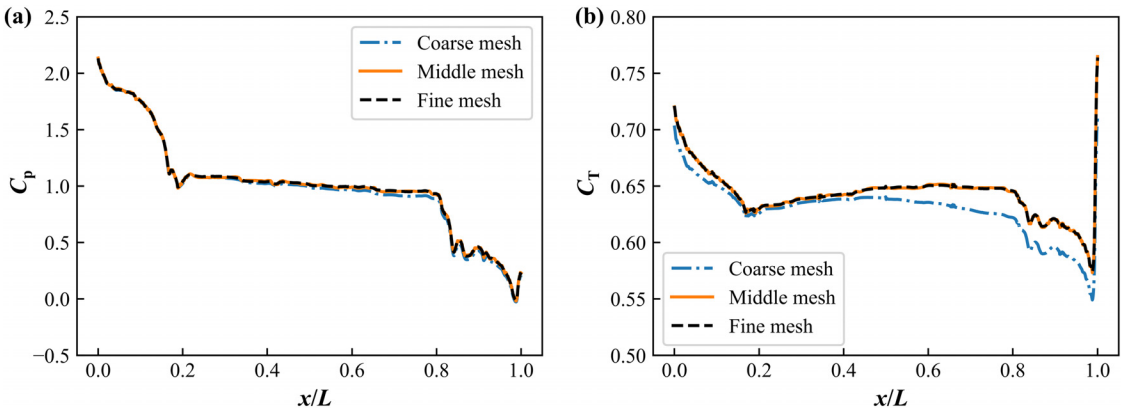

FIG. 3. Parameter values under different density of mesh: (a) C_p and (b) C_T (example at $Ma = 1.8$).

conditions. Consequently, this study references a wind tunnel trial on an ejector-based system performed at the Institute for Chemical Propulsion at the German Aerospace Center.[53,54] This experiment was numerically replicated using the methodologies outlined in Sec. II D. Figure 4(a) delineates the computational domain employed for this test, offering a robust reference for the numerical configurations utilized in the ETMT algorithm. The test section measures 0.3 m in length and 0.05 m in width, with a 3° expansion at 0.058 m from the top. The injector, featuring a wedge shape, has a length of 0.032 m and a tip angle of 12°, placed 0.035 m from the inlet and 0.025 m from the boundary, at the center of the test section's width. The operation pressure here is $p_{atm} = 1$ atm. The inflow at the test section's entrance has a Mach number of 2.0, closely aligned with the supersonic speeds tested in the ETMT.

This study replicated the wind tunnel's setup, using a similar computational domain and boundary conditions and employing the numerical algorithms and configurations as outlined in Sec. II D. Monitoring focused on the static pressure distribution along the x-direction at the centerline of the wind tunnel's sidewall, comparing it to the wind tunnel test data shown in Fig. 4(b). The results from the numerical simulations not only align closely with the experimental data in terms of numerical values but also follow similar trends, thereby confirming the accuracy and reliability of the numerical approaches used in this research. The Nash-Sutcliffe Efficiency coefficient (NSE) is employed here to evaluate the predictive accuracy of nonlinear quantitative fits. The formula is specified as

$$\mathrm{NSE} = 1 - \frac{\sum (y_i - f(x_i))^2}{\sum (y_i - \bar{y})^2}, \tag{7}$$

where $y_i = p/p_{atm}$, with $\bar{y}$ representing the average of y_i. The function $f(x)$ denotes the cubic spline data smoothing fit from CFD experimental results. Utilizing this formula, the NSE value computed for Fig. 4(b) is 0.87, indicating a substantial correspondence between the wind tunnel test outcomes and the CFD numerical simulations, which confirms the appropriateness of the CFD configurations.

IV. RESULTS AND DISCUSSION

A. Shockwave within the tube

Intriguing and complicated phenomena are present in the wake flow at the rear of the train, which differ significantly from those observed in the wake of traditional high-speed trains. This analysis delves into the wake flow dynamics of the ETMT operating at a speed of $Ma = 1.8$. Figure 5 delineates the wake flow topology along the vertical centerline plane ($Y = 0$), which accentuates asymmetry in the upper and lower portions of the wake.

Within the evacuated tube transport system, the space between the train and the tube can be regarded as a Laval nozzle. The

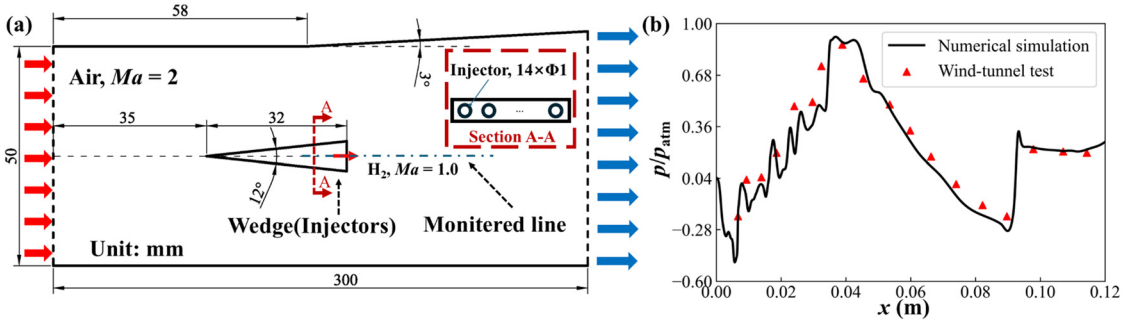

FIG. 4. Comparison of numerical simulation and wind tunnel test: (a) the geometric configuration and (b) the dimensionless pressure on monitored line.

09 January 2026 03:26:12

Published under an exclusive license by AIP Publishing

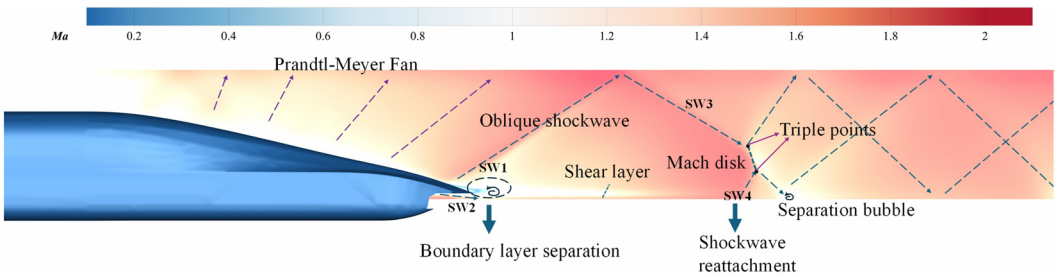

FIG. 5. Fundamental principles of shockwave formation (example at $Ma = 1.8$).

streamlined aft section of the train forms the divergent part of this nozzle, where the classical Prandtl–Meyer isentropic flows are most pronounced, particularly at the tail's apex.[55] This segment experiences accelerated airflow and a consequent decrease in pressure. Owing to substantial expansion, the pressure surrounding the tail dips below the ambient undisturbed pressure. Two oblique shockwaves, identified as SW1 and SW2 in Fig. 5, arise on the maglev train's dorsal and ventral surfaces. These shockwaves facilitate flow redirection and an elevation in pressure. SW1 interacts with the upper boundary of the tube, triggering a reflective wave, SW3. Moreover, the reverse pressure gradient instigated by SW1 and SW2 precipitates a flow separation at the tail tip, spawning a shear layer that intensifies the wake's unsteadiness and instability. This shear layer, upon reattaching to the ground wall, forms a reattachment shockwave, SW4, which thereafter progressively retreats from the ground. The area between SW3 and SW4 witnesses irregular intersections that culminate in the formation of triple points and a Mach disk. The boundary layer initially exhibits relatively minimal thickness, and progressing along the flow direction, the boundary layer on the train's surface incrementally thickens. Upon the airflow encountering the streamlined portion of the rear car, it undergoes acceleration due to expansion, resulting in a reduction of the boundary layer thickness. Additionally, when the shockwave engages the unstable shear layer, discernible separation bubbles emerge. Oblique shockwaves and expansion waves persistently reflect and propagate along the tube surfaces, countering to the train's motion. As the shockwaves and expansion waves' energies disperse due to air viscosity, their intensity wanes, leading to a gradual diffusion and an observable disparity in airflow velocities across the upper and lower regions, distinctly evident in the extended wake zone linked to the shear line.

As illustrated in Fig. 6(a), the interaction between expansion waves and shock waves results in a complex structure within the wake flow. The presence of Prandtl–Meyer flow in the annular gap at the rear of the train contributes to the formation of expansion waves. Upon contacting the tube wall, these expansion waves reflect and generate reflected waves, effectively reproducing the expansion waves. Concurrently, due to the separation of the boundary layer, oblique shock waves are also produced at the rear of the train; these waves reflect off the wall and give rise to additional oblique shock waves.[56] Previous research has indicated that shock waves exert a notable influence on the boundary layer, potentially leading to increased thickness in the viscous region and resulting in fluctuations in pressure and temperature amplitudes.[57] For instance, in Region I, the interaction between expansion waves and shock waves creates a pressure difference between Regions II and III. This pressure difference does not significantly alter the characteristics of the wave system following the interaction, meaning that it does not substantially affect the downward trend of pressure and temperature. However, when the expansion waves interact along the centerline, an increase in air speed occurs, accompanied by a corresponding decrease in temperature and pressure. Subsequently, as the oblique shock waves reconvene, the Mach

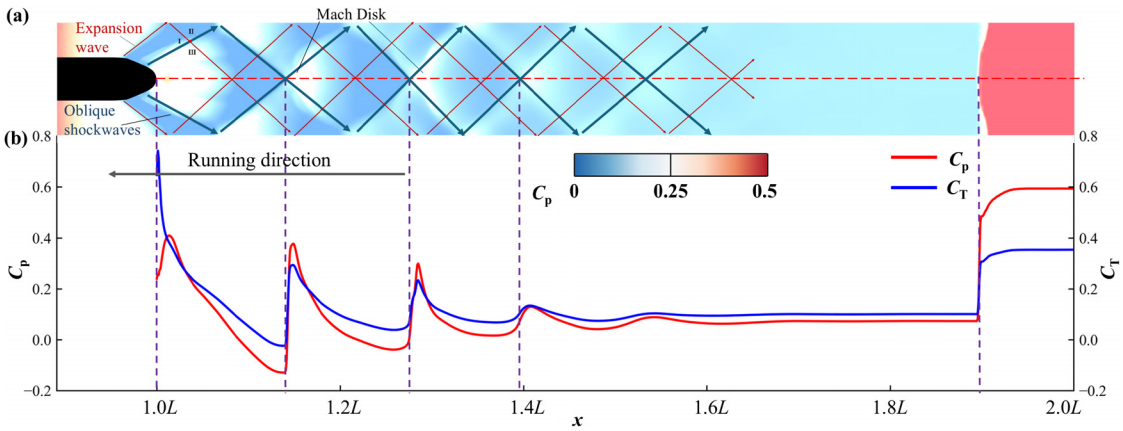

FIG. 6. The structure of the wake at the train tail with Ma = 1.8: (a) Schematic of the interaction of the shockwaves and expansion waves as well as (b) C_p and C_T along moving directions.

09 January 2026 03:26:12

Published under an exclusive license by AIP Publishing

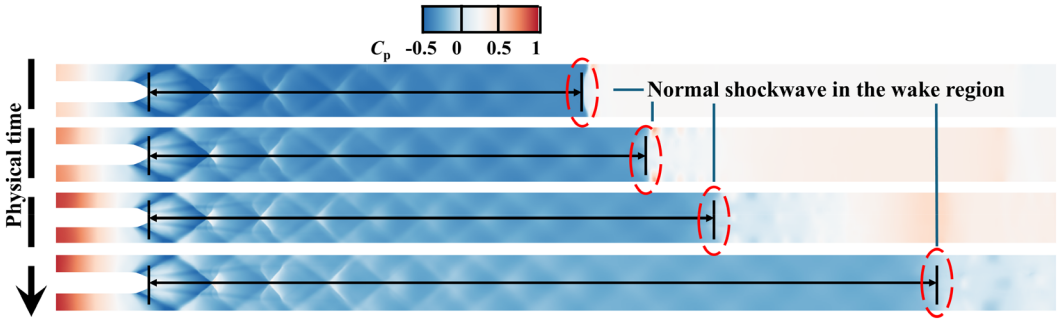

FIG. 7. Propagation of normal shockwave in the wake region of the ETMT (example at $Ma = 1.2$).

disk, characterized by irregular reflections, emerges near the axis, with shock waves reflecting off the wall upon encountering the Mach disk. Figure 6(a) also reveals significant diamond-shaped structures resulting from various wave interactions within the train's wake. Under the influence of viscosity at the interface between the wall and the air, these diamond structures gradually dissipate, yielding unit structures representative of shock waves and expansion waves. The behavior of these unit structures holds important physical implications, with rectangular units indicating shock compression and circular units denoting expansion.[58] Analysis of the jet reveals that the C_p values and C_T values in Fig. 6(b) highlight fluctuations of local maxima and minima along the centerline. These fluctuations can be attributed to wave interactions, where peaks occur in proximity to shock wave interactions, while troughs are associated with expansion wave interactions. In supersonic flows, a shockwave front emerges when airflow speed undergoes a rapid transition from supersonic to subsonic, as depicted in Fig. 7. As the train operates at sonic speeds, the normal shockwave propagates progressively farther from the vehicle, advancing at subsonic velocities. Over time, the post-shock flow field approaches a new state of equilibrium, the pressure gradient within the space gradually diminishes, and the delineation of the normal shockwave boundary becomes progressively indistinct.

Figure 8(a) showcases pressure contour maps for various Mach numbers across different cross sections. At $Ma = 0.8$, the front of the train exhibits minimal pressure buildup, with no wave structures detected surrounding the tube. As the Mach number reaches 1.0, pressure accumulation becomes prominent at the front of the train, intensifying with increasing Mach numbers. The pressure seamlessly transitions from the train's nose to its body. A vivid shockwave phenomenon emerges at the rear, with shockwaves bouncing between the tube walls, weaving a complex pattern of intersections. Due to the tube's three-dimensional configuration, dual shockwaves form at the juncture of the train's shoulder and tail, projecting toward the tube walls. These shockwaves, upon hitting the walls, reflect back, forming intersecting shockwaves at the tube's core and weaving an intricate mesh of wave interactions. These intersecting waves persistently reflect and extend toward the outlet, steadily losing strength. Moreover, the wake of the maglev train displays significant fluctuations, markedly influencing the shockwave array. Figure 8(b) depicts the pressure contour maps along the longitudinal sections for different Mach numbers. At $Ma = 0.8$, the train's front shows no signs of pressure buildup. By $Ma = 1.0$, a buildup of pressure commences, escalating as the train's speed increases. Notably, sharp shockwaves begin to manifest, intensifying with the train's velocity. The wake of the train reveals a considerably more intricate flow compared to its front. The train and the tube collectively function akin to a Laval nozzle, with the wake serving as the expansion section, where Prandtl–Meyer expansion fans emerge, accelerating the airflow and decreasing the pressure to create slanting shockwaves within the tube. As the train accelerates, the Laval nozzle effect becomes increasingly pronounced. Furthermore, as the maglev train hurtles through the evacuated tube, the limited space above the track and beneath the tube complicates the flow dynamics. Shockwaves predominantly populate this area, forming a cone reminiscent of a trumpet, with the apex situated at the rear nose of the maglev train. The upper region of this cone is distinctly more pronounced, while the bottom, shaped by the maglev track's influence, remains

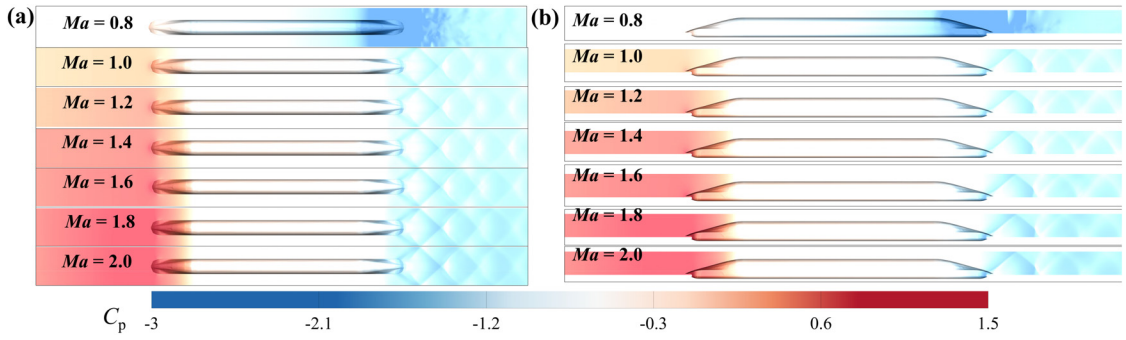

FIG. 8. Pressure distribution inside the tube under different Mach numbers: (a) the top view and (b) the side view.

09 January 2026 03:26:12

Published under an exclusive license by AIP Publishing

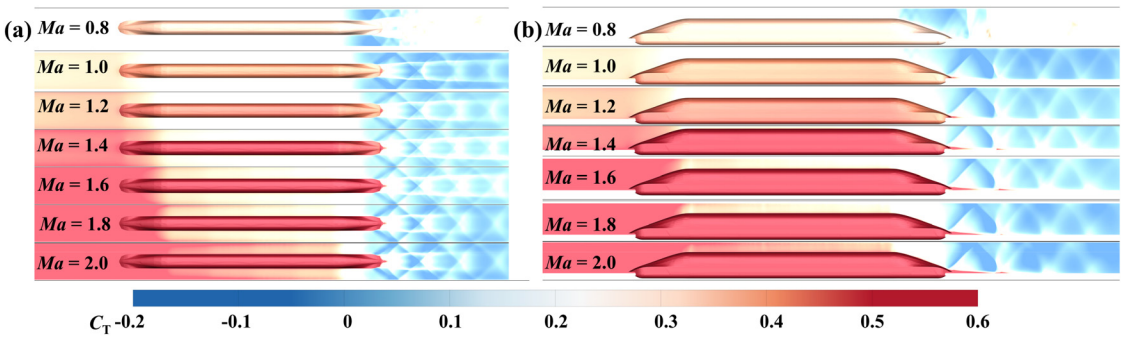

FIG. 9. Temperature distribution inside the tube under different Mach numbers: (a) the top view and (b) the side view.

nearly flat. These shockwaves extend toward the tube walls, where they reflect and crisscross, creating a diminishing yet complex array of shockwave patterns stretching toward the tube's exit.

Aerodynamic heating arises from the compression of air around swiftly moving objects, wherein the airflow's kinetic energy is transformed into thermal energy. A thorough examination of how temperature and pressure distributions interact with the train's dynamic and the directional airflow within the tube's annular space is critical. Figures 9(a) and 9(b) illustrate temperature contours in both cross-sectional and longitudinal sections. At a Mach number of 0.8, there is neither temperature build up at the train's front nor notable shockwave activity at its rear. However, as the incoming Mach number escalates, so does the intensity of the high-temperature zones at the train's forefront. Air near the train's nose accumulates and undergoes intense compression. By the time the Mach number reaches 1.0, significant temperature accumulation manifests at the front, intensifying with the train's increasing velocity. Concurrently, pronounced shockwave phenomena emerge at the train's rear, which grow more distinct with greater speeds. The airflow dynamics in the wake of the train is substantially more intricate. A complex sequence of shock waves initiates, develops, and dissipates around the rear car, leading to intricate temperature fluctuations in the surrounding airflow. Near the nose tip of the rear car, a zone of reduced temperature forms, influenced by adverse pressure gradients that induce temperature separation within the boundary layer, resulting in a vortex structure at this location. As the train advances, a distinct pattern of diamond-shaped shock waves becomes evident in the wake. These shock waves, influenced by the rear car's expansion waves, gradually dissipate as energy is dissipated, while new diamond wave structures continuously evolve. Influenced by these expansion waves, the temperature boundary layer along the car's body narrows at the shoulders before thickening. Together, the train and the tube effectively form a Laval nozzle, with the wake area acting as the expansion section. This area witnesses Prandtl–Meyer expansion fans, which accelerate the airflow and lower the temperature, creating extensive areas of reduced temperature and generating oblique shockwaves within the tube. The manifestations of the Laval nozzle effect become more pronounced as the train accelerates.

B. Surface pressure coefficient analysis

Special focus is directed toward the variations in surface pressure coefficients. The train is segmented into three distinct areas based on its cross-sectional changes: the streamlined head region ($0 < x/L < 0.2$), which functions as a contraction zone; the body region ($0.2 < x/L < 0.8$); the site of boundary layer development; and the streamlined tail region ($0.8 < x/L < 1.0$), an expansion area. As depicted in Fig. 10(a), in the streamlined head section, extending up to $x/L = 0.16$, there is a gradual decrease in the pressure coefficient in the direction of train travel. Notably, at $x/L = 0.16$, where the streamlined head intersects with the body section, the pressure coefficient dips to a minimum, followed by slight fluctuations near this juncture. The body section witnesses a continued decline in the pressure coefficient,

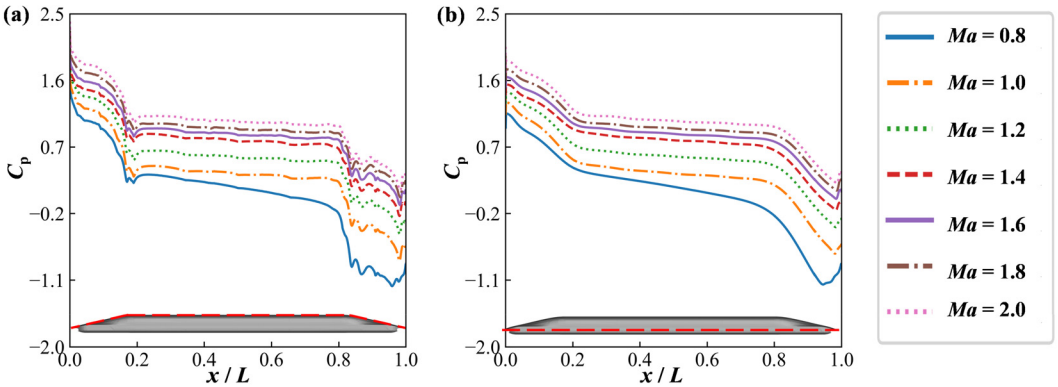

FIG. 10. Pressure distribution along axis x at (a) the top of the train and (b) the bottom of the train.

09 January 2026 03:26:12

Published under an exclusive license by AIP Publishing

although the rate of this decline moderates, especially at higher speeds with Mach numbers from 1.00 to 2.00, where the fluctuations in the pressure coefficient begin to stabilize. At Mach 0.8, the reduction in the pressure coefficient is more marked. Within the tail's streamlined section, the pressure coefficient is significantly affected by shockwaves, leading to persistent fluctuations. These fluctuations reflect the intense shockwave activities at the train's tail and the dynamic reflections and interactions of shockwaves against the tube walls.

A detailed analysis of the maglev train's underside pressure coefficients is also depicted in Fig. 10(b), where the red dashed line clearly delineates the pressure coefficient trends along the train's position x/L. This analysis, covering various segments from the train's front to its rear, zeroes in on the aerodynamic behaviors under differing Mach numbers. From $0 < x/L < 0.2$, irrespective of the Mach number, the pressure coefficients decrease, indicating a reduction in pressure at the train's front underside due to aerodynamic effects, regarded as a characteristic of the Laval nozzle, linked to accelerated airflow and minimal flow resistance. The presence of the track further narrows the internal space of the tube, exacerbating the choked flow at the train's front underside. Observations in the midsection, $0.2 < x/L < 0.8$, under Mach numbers between 1.00 and 2.00, show that although the pressure coefficient continues to decrease, this decrease significantly slows and nearly stabilizes, due to mature boundary layer development creating smoother flow dynamics. At $Ma = 0.8$, the pressure coefficient not only continues to decrease but also does so at an increased rate, reflecting more pronounced aerodynamic effects at lower speeds. In the rear section, where $0.8 < x/L < 0.9$, the pressure coefficient exhibits a more pronounced decline due to the dynamic flow characteristics prevalent in the train's extended tail region. The airflow in this region either accelerates or encounters complex separations, as depicted in Fig. 5. This segment acts as the genesis zone for the Prandtl–Mayer Fan, characterized by the emergence of expansion waves. These waves precipitate a reduction in both pressure and temperature, thereby generating gases with increased velocities. In the terminal section, where $0.9 < x/L < 1.0$, the pressure coefficient initially declines before experiencing a sharp rise, establishing a local minimum. This dynamic is linked to variations in the Mach number, with higher Mach numbers intensifying the observed minimum. This behavior is primarily due to the interactions between the shock waves emanating from the train's tail and the boundary layer. Following this, there is an increase in pressure triggered by the formation of an oblique shock wave at the train's nose, as illustrated in Fig. 5, precipitating a notable escalation in both pressure and temperature values.

C. Surface temperature coefficient analysis

The temperature dynamics within the tube is heavily influenced by wave phenomena, particularly the shockwave-induced heating of the air surrounding the train. Furthermore, the train endures significant frictional heating within its surface boundary layer, an effect amplified by the sealed, evacuated nature of the tube, thereby exacerbating the aerodynamic heating. Consistently across various x/L ratios, the surface velocity of the train increases with its speed. Initially, the air at the train's front end is rapidly compressed, resulting in a temperature rise—this is explained by the ideal gas law, where pressure and temperature are directly proportional, a scenario commonly observed in aircraft and other high-speed vehicles. Moreover, the friction between the airflow and the train's surface generates considerable heat. As the ETMT races against air molecules, substantial heat is produced. With increasing speeds, this friction-induced heat intensifies, leading to an elevation in surface temperature.

As is shown in Fig. 11, on the $Y = 0$ plane, intersecting the top surface of the train, the section from $0 < x/L < 0.2$ represents the train's aerodynamically streamlined head, where surface temperatures sharply decline along the direction of travel. From $0.2 < x/L < 0.8$, although the surface temperature continues to fall, the rate of decrease is slower compared to the contraction zone at the train's head. This moderation in temperature drop is due to the diminishing flow area caused by the development of the boundary layer, where both the streamlined head and the straight body act as contraction zones—the former through geometric changes and the latter due to changes in physical flow dynamics. In the streamlined tail section, influenced by Prandtl–Meyer expansion fans depicted in Fig. 5, the temperature gradually decreases from $0.8 < x/L < 1.0$. In this section, the surface temperature initially reduces gradually with minor fluctuations, and then near $x/L = 1.0$, it suddenly spikes to its maximum due to the effects of oblique shockwaves. The airflow at the train's tail becomes extremely complex, creating localized high temperatures. As this area acts as an expansion section, the airflow accelerates to supersonic speeds until it encounters a shockwave, which then slows the airflow, causing both temperature and pressure to rise.

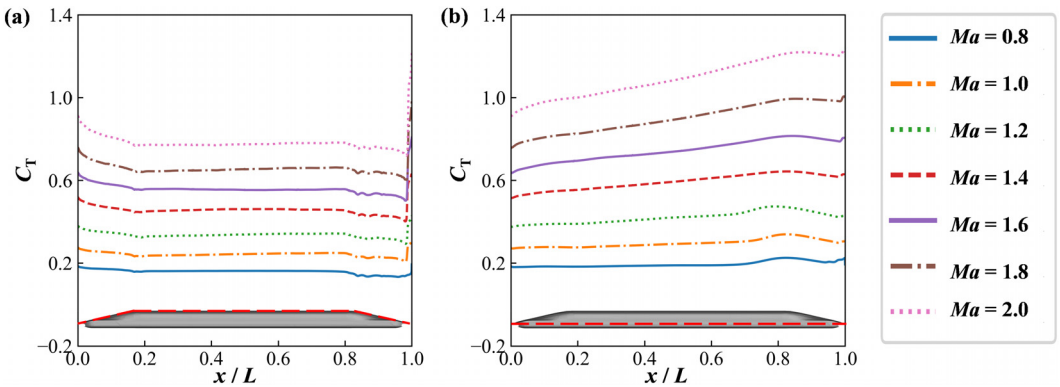

FIG. 11. Temperature distribution along axis x at (a) the top of the train and (b) the bottom of the train.

09 January 2026 03:26:12

Published under an exclusive license by AIP Publishing

This study also reviews the maglev train's streamlined underside, a simplified area with a small cross-sectional profile. Within the $0 < x/L < 0.8$ range, the temperature steadily increases in the direction of the train's movement, reaching a peak at $x/L = 0.8$. This peak results from a congestion effect prevalent at high speeds, leading to continuous energy accumulation. From $0.8 < x/L < 1.0$, the temperature slightly decreases in the direction of travel, with a sudden fluctuation at $x/L = 1.0$. This temperature variability is triggered by oblique shockwaves and expansion waves (shown in Figs. 5 and 6); at points where the shockwave intersects with the train's tail surface and where boundary layer separation occurs, there is a localized increase in temperature.

An additional critical aspect of the flow behavior near the rear of the train is the flow separation resulting from the interaction between the curvature of the train's surface and the shock wave and the boundary layer. The presence of the shock wave intensifies the adverse pressure gradient, thereby facilitating flow separation. As illustrated in Fig. 12, the separation of airflow around the tail of the train creates a region of elevated temperature. An analysis was performed on the flow variables represented by the red line at a position 0.0125 L from the train's tail. From the centerline to point A, the temperature remains consistently high within the flow region, whereas the pressure experiences a significant decrease, progressively reaching its maximum rate of decline. In the region away from the centerline, the temperature exhibits a marked decrease, while the pressure diminishes relatively slowly from point A to point B and then shows a slight recovery near point B, resulting in a small local maximum. Subsequently, the pressure begins to decrease gradually, while the temperature experiences a sharp decrease, with the rate of reduction gradually diminishing. These flow variables then stabilize slowly until they reach the shock waves at points C and D, at which point the flow characteristics undergo further gradual changes. Furthermore, Fig. 12 indicates that when the Mach number (Ma) is equal to or greater than 1.0, the formation of shock waves aligns closely with the trends observed in the dimensionless flow variables. Conversely, at $Ma = 0.8$, the trends of the flow variables display notable differences, primarily due to the fact that, under these conditions, the shock wave is still in the process of formation and has not yet fully developed.

D. Aerodynamic load analysis

This analysis delves into the aerodynamic loads impacting various sections of the train, with specific reference to Tables III and IV, which detail the average drag and lift coefficients under diverse operational scenarios. Table III reveals that the majority of the train's total drag comprises pressure drag and friction drag, with pressure drag predominating, accounting for about 80% of the total. This significant pressure drag results primarily from the shockwaves generated in the tube as the train operates at high velocities. These shockwaves create a substantial pressure differential between the train's front and rear, manifesting as pronounced shockwave-induced drag. Figure 13(a) indicates that the head car contributes most significantly to the total drag coefficient, followed by the tail car at higher Mach numbers ($Ma > 1.4$) and the middle car at lower Mach numbers ($Ma < 1.4$).

A closer examination of Table III and Fig. 13(a) provides detailed insights into the variations in aerodynamic drag across the head,

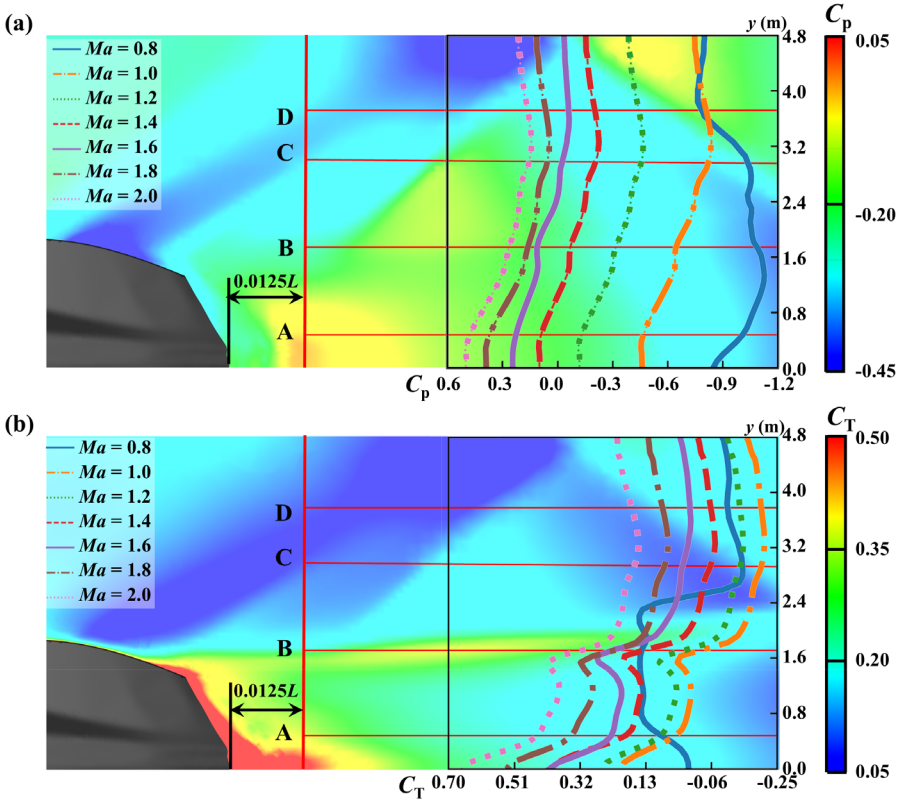

FIG. 12. Contours of C_p (a) and C_T (b) at the train rear for $Ma = 1.8$, along with the distribution of C_p (a) and C_T (b) at a distance of 0.0125 L from the tail for various Mach numbers.

09 January 2026 03:26:12

Published under an exclusive license by AIP Publishing

TABLE III. Average drag coefficient of different train parts.

	Head carriage			Middle carriage			Tail carriage			Total train		
Case	C_{dp}	C_{df}	C_d	C_{dp}	C_{df}	C_d	C_{dp}	C_{df}	C_d	C_{dp}	C_{df}	C_d
$Ma = 0.80$	0.921	0.200	1.121	0	0.177	0.177	1.030	0.204	1.234	1.951	0.582	2.532
$Ma = 1.00$	1.081	0.177	1.258	0	0.152	0.151	0.554	0.18	0.734	1.634	0.508	2.143
$Ma = 1.20$	1.252	0.16	1.412	0	0.137	0.137	0.208	0.16	0.367	1.459	0.457	1.917
$Ma = 1.40$	1.366	0.147	1.513	0	0.125	0.125	−0.013	0.146	0.133	1.353	0.418	1.772
$Ma = 1.60$	1.475	0.144	1.619	0	0.126	0.126	−0.16	0.142	−0.018	1.315	0.413	1.727
$Ma = 1.80$	1.582	0.142	1.725	0	0.125	0.125	−0.281	0.14	−0.14	1.302	0.407	1.709
$Ma = 2.00$	1.686	0.142	1.827	0	0.123	0.123	−0.385	0.14	−0.246	1.301	0.404	1.705

TABLE IV. Average lift coefficient of different train parts.

Case	Head carriage	Middle carriage	Tail carriage	Total train
$Ma = 0.80$	0.027	0.034	0.789	0.85
$Ma = 1.00$	0.022	0.028	0.611	0.661
$Ma = 1.20$	0.01	0.027	0.544	0.581
$Ma = 1.40$	0.015	0.025	0.501	0.542
$Ma = 1.60$	−0.003	0.027	0.496	0.521
$Ma = 1.80$	−0.006	0.029	0.497	0.52
$Ma = 2.00$	0	0.028	0.497	0.525

middle, and tail cars at different speeds. Specifically, as the train speed increases, the aerodynamic drag on the head car rises substantially. With the Mach number increasing from 0.8 to 2.0, the drag coefficient of the Head Carriage rises by approximately 83%, primarily due to an increasing pressure differential on both sides of the head car. Conversely, the drag on the tail car escalates at a more accelerated rate than that on the head car; as the Mach number shifts from 0.8 to 2.0, the drag coefficient of the Tail Carriage increases by about 120%. This trend is attributed to the lower-pressure zone enveloping the tail car, which is comparatively less influenced by the external pressure differentials. Meanwhile, the aerodynamic drag on the middle car remains relatively stable, decreasing by approximately 30% as speed increases, suggesting a weaker influence from airflow forces and a primary contribution from frictional drag. Moreover, there is a consistent reduction in the drag coefficient C_d as the Mach number progresses from 0.8 to 1.8, resulting in a net reduction of 32%. Yet, upon escalating from 1.8 to 2.0, the drag coefficient plateaus, while the incremental efficiency benefits are mitigated by the augmented aerodynamic heating and pressure drag resultant from exceedingly high velocities. Consequently, it is deduced that a $Ma = 1.8$ optimizes the decrement in drag coefficient, thereby constituting the most economically viable velocity for the train.

Table IV further examines the average lift coefficient, highlighting distinct vertical aerodynamic behaviors across different sections of the train. Unlike the distribution of drag, the lift coefficients between the leading and tail cars display marked variation, with the tail car demonstrating a considerably higher lift coefficient, particularly at elevated

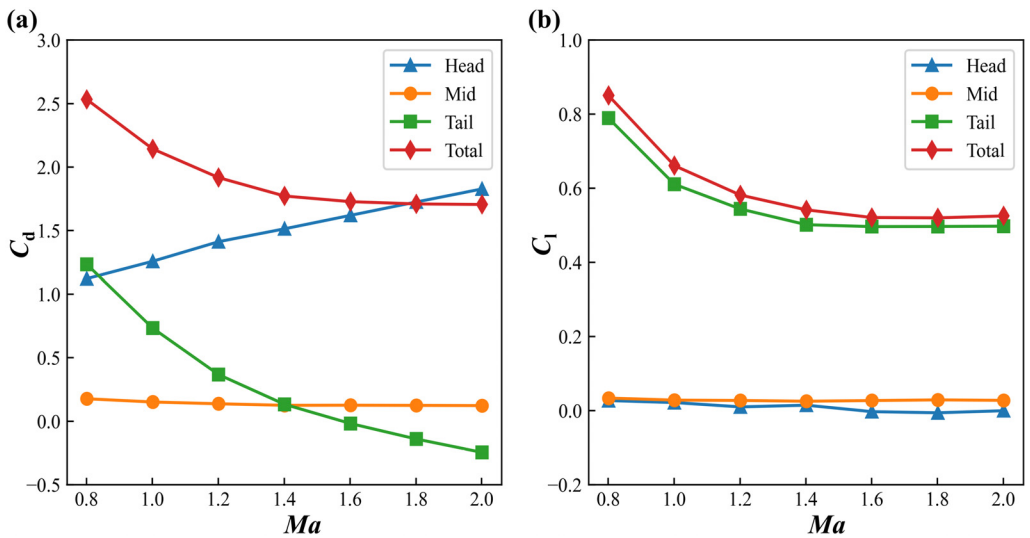

FIG. 13. Aerodynamic loads under different Mach numbers: (a) drag coefficient C_d and (b) lift coefficient C_l.

09 January 2026 03:26:12

Published under an exclusive license by AIP Publishing

speeds. This discrepancy may be linked to flow separation at the rear of the train, where a low-pressure region forms above the tail car, enhancing its lift. As the Mach number rises from 0.8 to 2.0, the lift on the tail car decreases by approximately 38%, while the lift for the leading and middle cars remains nearly constant. As presented in Table IV and Fig. 13(b), the lift on the tail car is overwhelmingly dominant, accounting for over 90% of the total lift under various conditions, while the lift on the leading and middle cars remains relatively minor. This substantial lift on the tail car can be attributed to a pronounced pressure differential between its upper and lower surfaces, induced by flow separation. As the train speed increases, the aerodynamic lift on the leading and middle cars remains relatively constant, while the lift on the tail car gradually decreases, resulting in a continued reduction in overall train lift. This decrease in lift is primarily due to intensified interactions between shockwaves and boundary layers near the tail car, leading to more prominent flow separation and a subsequent reduction in lift, a phenomenon commonly referred to as "shockwave stall."

V. CONCLUSION

This research explored the shockwave structure in the tube as well as the fluid dynamics behaviors of maglev trains within tubes at varying Mach numbers, particularly focusing on changes in pressure and temperature distributions as well as aerodynamic loads on the train. The results clearly demonstrate the substantial impact of Mach numbers on the train's aerodynamic properties, summarized in several key findings:

(1) Complex interactions between expansion waves and shock waves appear at the rear of ETMT, including the formation of distinctive diamond-shaped structures and fluctuations in pressure and temperature. Changes in flow behavior, such as flow separation and shockwave interactions, impact the flow variables near the train's tail, leading to variations in temperature and pressure along specific points.
(2) At Mach numbers of 1.0 or greater, there is a significant buildup of pressure at the train's front, which becomes more pronounced as Mach numbers increase. Additionally, the shockwave effects in the tail region intensify with speed, as shockwaves reflect off the tube walls and intersect in the center, creating complex interactions.
(3) The temperature distribution is notably influenced by the increase in Mach numbers, especially at the rear of the train where higher speeds lead to more severe temperature accumulations. Furthermore, the interaction between the train and the tube induces a Laval nozzle effect, significantly lowering temperatures in the wake region.
(4) The analysis reveals that pressure differential drag, especially at the train's front and rear, dominates the overall drag, particularly under high Mach numbers. Upon an increase in the Mach number from 0.8 to 2.0, the drag coefficient of the head carriage rose by 83%, whereas it fell by 30% for the middle carriage and surged by 120% for the tail carriage, resulting in a net reduction of 32% in the total train drag coefficient. A Mach number of 1.8 is the most economically viable velocity for the train. The aerodynamic characteristics between the train's top and bottom surfaces differ significantly, showing diverse distributions of temperature and pressure coefficients, largely due to variations in flow separation and boundary layer development.
(5) The tail carriage's aerodynamic drag and lift are crucial to the train's overall performance, with the majority of the lift concentrated at the tail. Remarkably, as the Mach number increases, the lift of the tail carriage diminished by 38%, with the lift coefficients of the middle and head carriages remaining essentially stable, a behavior often linked to shockwave stalls.

Considering these detailed observations, a relatively simplistic model of a maglev train and track system is introduced, positioning it as a foundational step for subsequent design developments. There exists considerable scope for the refinement of the aerodynamic profile, pertinent to practical engineering applications. Moreover, future endeavors could explore the interplay between the aerodynamics of the train and its structural responses, aiming to bolster the operational stability of the ETMT within engineering contexts.

ACKNOWLEDGMENTS

This work was supported by the following projects: the Key Project of Basic and Applied Basic Research of Jiangmen (Grant No. JZ202201), the Hong Kong and Macau Joint Research and Development Fund of Wuyi University (Grant No. 2021WGALH15) and China Academy of Railway Sciences Corporation Limited Research Project (Grant No. 2022YJ139).

AUTHOR DECLARATIONS

Conflict of Interest

The authors have no conflicts to disclose.

Author Contributions

Zun-Di Huang: Conceptualization (equal); Funding acquisition (equal); Methodology (equal); Project administration (equal). **Cheng Peng:** Formal analysis (equal); Software (equal); Visualization (equal); Writing – original draft (equal). **Zheng-Wei Chen:** Supervision (equal); Validation (equal); Writing – review & editing (equal). **Zi-Jian Guo:** Resources (equal); Visualization (equal). **Ning Chang:** Writing – review & editing (equal). **Hong-Bei Chen:** Software (equal). **Wei-Kai Kong:** Software (equal). **You-Biao Wang:** Resources (equal).

DATA AVAILABILITY

The data that support the findings of this study are available from the corresponding author upon reasonable request.

REFERENCES

[1]H.-W. Lee, K.-C. Kim, and L. Ju, "Review of maglev train technologies," IEEE Trans. Magn. **42**, 1917 (2006).
[2]Z.-J. Guo, Z.-H. Guo, Z.-W. Chen, G.-Z. Zeng, and J.-Q. Xu, "On the active flow control in maglev train safety under crosswinds: Analysis of leeward suction and blowing action," Phys. Fluids **36**, 095130 (2024).
[3]K. van Goeverden, D. Milakis, M. Janic, and R. Konings, "Analysis and modelling of performances of the HL (Hyperloop) transport system," Eur. Transp. Res. Rev. **10**, 41 (2018).
[4]M. Janić, "Estimation of direct energy consumption and CO_2 emission by high speed rail, transrapid maglev and hyperloop passenger transport systems," Int. J. Sustainable Transp. **15**, 696 (2021).

09 January 2026 03:26:12

Published under an exclusive license by AIP Publishing

[5]Q. L. Li, W. G. Jia, C. G. Dong, and R. X. Duan, "Numerical research of thermal-pressure coupling effect on blockage ratio in the evacuated tude transportation system," Key Eng. Mater. **561**, 454 (2013).
[6]Z. Deng, W. Zhang, J. Zheng, B. Wang, Y. Ren, X. Zheng, and J. Zhang, "A high-temperature superconducting maglev-evacuated tube transport (HTS Maglev-ETT) test system," IEEE Trans. Appl. Supercond. **27**, 1 (2017).
[7]T. Goudon, P. Lafitte, and C. Mascia, "Shock profiles for hydrodynamic models for fluid-particles flows in the flowing regime," Phys. D **470**, 134357 (2024).
[8]Z.-J. Guo, Z.-W. Chen, Z.-X. Che, A. Bordbar, and Y.-Q. Ni, "Using leeward air-blowing to alleviate the aerodynamic lateral impact of trains at diverse yaw angles," Phys. Fluids **36**, 045121 (2024).
[9]G.-Z. Zeng, Z.-W. Chen, Y.-Q. Ni, and E.-Z. Rui, "Investigating embedded data distribution strategy on reconstruction accuracy of flow field around the crosswind-affected train based on physics-informed neural networks," Int. J. Numer. Methods Heat Fluid Flow **34**, 2963 (2024).
[10]Z. W. Chen, Z. H. Guo, Y. Q. Ni, Z. J. Guo, T. T. Wang, E. Z. Rui, and G. Z. Zeng, "Parametric investigation of suction actuators on the tunnel wall for alleviating pressure interactions in high-speed maglev train/tunnel system," Tunnelling Underground Space Technol. **156**, 106239 (2025).
[11]X. Chen, S. Zhong, T. Liu, J. Zhang, O. Ozer, and G. Gao, "Experimental study on the synergy of sweeping jets on the afterbody flows of a slanted-base cylinder," Aerosp. Sci. Technol. **148**, 109096 (2024).
[12]S. A. Gillani, V. P. Panikulam, S. Sadasivan, and Z. Yaoping, "CFD analysis of aerodynamic drag effects on vacuum tube trains," J. Appl. Fluid Mech. **12**, 303 (2019).
[13]Y. Seo, M. Cho, D. H. Kim, T. Lee, J. Ryu, and C. Lee, "Experimental analysis of aerodynamic characteristics in the Hyperloop system," Aerosp. Sci. Technol. **137**, 108265 (2023).
[14]Z. Hou, Y. Zhu, J. Bo, and J. Yang, "A quasi-one-dimensional study on global characteristics of tube train flows," Phys. Fluids **34**, 026104 (2022).
[15]Z.-W. Chen, Z.-H. Guo, Y.-Q. Ni, T.-H. Liu, and J. Zhang, "A suction method to mitigate pressure waves induced by high-speed maglev trains passing through tunnels," Sustainable Cities Soc. **96**, 104682 (2023).
[16]Y. Sui, J. Niu, P. Ricco, Y. Yuan, Q. Yu, X. Cao, and X. Yang, "Impact of vacuum degree on the aerodynamics of a high-speed train capsule running in a tube," Int. J. Heat Fluid Flow **88**, 108752 (2021).
[17]R. Li, D. Soper, J. Xu, Y. Jia, J. Niu, and H. Hemida, "A separated-flow model for 2-D viscous flows around bluff bodies using the panel method," Appl. Sci. **12**, 9652 (2022).
[18]Z.-W. Chen, E.-Z. Rui, T.-H. Liu, Y.-Q. Ni, X.-S. Huo, Y.-T. Xia, W.-H. Li, Z.-J. Guo, and L. Zhou, "Unsteady aerodynamic characteristics of a high-speed train induced by the sudden change of windbreak wall structure: A case study of the Xinjiang Railway," Appl. Sci. **12**, 7217 (2022).
[19]X. Li, G. Chen, D. Zhou, and Z. Chen, "Impact of different nose lengths on flow-field structure around a high-speed train," Appl. Sci. **9**, 4573 (2019).
[20]Q. Yu, X. Yang, J. Niu, Y. Sui, Y. Du, and Y. Yuan, "Theoretical and numerical study of choking mechanism of fluid flow in Hyperloop system," Aerosp. Sci. Technol. **121**, 107367 (2022).
[21]S. Zhong, B. Qian, M. Yang, F. Wu, T. Wang, C. Tan, and J. Ma, "Investigation on flow field structure and aerodynamic load in vacuum tube transportation system," J. Wind Eng. Ind Aerodyn. **215**, 104681 (2021).
[22]K. S. Jang, T. T. G. Le, J. Kim, K.-S. Lee, and J. Ryu, "Effects of compressible flow phenomena on aerodynamic characteristics in Hyperloop system," Aerosp. Sci. Technol. **117**, 106970 (2021).
[23]M. Bizzozero, Y. Sato, and M. A. Sayed, "Aerodynamic study of a Hyperloop pod equipped with compressor to overcome the Kantrowitz limit," J. Wind Eng. Ind Aerodyn. **218**, 104784 (2021).
[24]K. Zhou, G. Ding, Y. Wang, and J. Niu, "Aeroheating and aerodynamic performance of a transonic hyperloop pod with radial gap and axial channel: A contrastive study," J. Wind Eng. Ind Aerodyn. **212**, 104591 (2021).
[25]X. Hu, Z. Deng, J. Zhang, and W. Zhang, "Effect of tracks on the flow and heat transfer of supersonic evacuated tube maglev transportation," J. Fluids Struct. **107**, 103413 (2021).
[26]W. Jia, K. Wang, A. Cheng, X. Kong, X. Cao, and Q. Li, "Air flow and differential pressure characteristics in the vacuum tube transportation system based on pressure recycle ducts," Vacuum **150**, 58 (2018).
[27]J. Niu, Y. Sui, Y. Qiujun, C. Xiaoling, Y. Yanping, and Y. Xiaofeng, "Effect of acceleration and deceleration of a capsule train running at transonic speed on the flow and heat transfer in the tube," Aerosp. Sci. Technol. **105**, 105977 (2020).
[28]P. Zhou, J. Zhang, T. Li, and W. Zhang, "Numerical study on wave phenomena produced by the super high-speed evacuated tube maglev train," J. Wind Eng. Ind Aerodyn. **190**, 61 (2019).
[29]I. Ali, S. Becker, J. Utzmann, and C.-D. Munz, "Aeroacoustic study of a forward facing step using linearized Euler equations," Phys. D **237**, 2184 (2008).
[30]X. Hu, Z. Deng, and W. Zhang, "Effect of cross passage on aerodynamic characteristics of super-high-speed evacuated tube transportation," J. Wind Eng. Ind Aerodyn. **211**, 104562 (2021).
[31]J.-S. Oh, T. Kang, S. Ham, K.-S. Lee, Y.-J. Jang, H.-S. Ryou, and J. Ryu, "Numerical analysis of aerodynamic characteristics of hyperloop system," Energies **12**, 518 (2019).
[32]Z. Guo, X. Chen, T. Liu, Z. Chen, and A. Bordbar, "Turbulence approaches for numerical predictions of vehicle-like afterbody vortex flows," Int. J. Mech. Sci. **283**, 109667 (2024).
[33]S. Alzhrani, M. M. Abdulla, K. Juhany, and I. AlQadi, "Numerical investigation of jet-propelled multiple-vehicle hyperloop system considering the suspension gap," Sustainability **16**, 9465 (2024).
[34]P. Zhou and J. Zhang, "Aerothermal mechanisms induced by the super high-speed evacuated tube maglev train," Vacuum **173**, 109142 (2020).
[35]Y. Sui, J. Niu, Y. Yuan, Q. Yu, X. Cao, D. Wu, and X. Yang, "An aerothermal study of influence of blockage ratio on a supersonic tube train system," J. Therm. Sci. **31**, 529 (2022).
[36]S. Bao, X. Hu, J. Wang, T. Ma, Y. Rao, and Z. Deng, "Numerical study on the influence of initial ambient temperature on the aerodynamic heating in the tube train system," Adv. Aerodyn. **2**, 28 (2020).
[37]T.-K. Kim, K.-H. Kim, and H.-B. Kwon, "Aerodynamic characteristics of a tube train," J. Wind Eng. Ind Aerodyn. **99**, 1187 (2011).
[38]Z.-W. Chen, G.-Z. Zeng, Y.-Q. Ni, T.-H. Liu, J.-Q. Niu, and H. D. Yao, "Reducing the aerodynamic drag of high-speed trains by air blowing from the nose part: Effect of blowing speed," J. Wind Eng. Ind Aerodyn. **238**, 105429 (2023).
[39]X.-S. Huo, T.-H. Liu, Z.-W. Chen, W.-H. Li, J.-Q. Niu, and H.-R. Gao, "Aerodynamic characteristics of double-connected train groups composed of different kinds of high-speed trains under crosswinds: A comparison study," Alexandria Eng. J. **64**, 465 (2023).
[40]J. Niu, Y. Sui, Q. Yu, X. Cao, and Y. Yuan, "Numerical study on the impact of Mach number on the coupling effect of aerodynamic heating and aerodynamic pressure caused by a tube train," J. Wind Eng. Ind Aerodyn. **190**, 100 (2019).
[41]T. T. G. Le, K. S. Jang, K.-S. Lee, and J. Ryu, "Numerical investigation of aerodynamic drag and pressure waves in hyperloop systems," Mathematics **8**, 1973 (2020).
[42]M. J. Colbrook, "Another look at residual dynamic mode decomposition in the regime of fewer snapshots than dictionary size," Phys. D **469**, 134341 (2024).
[43]"Railway applications–aerodynamics-Part4: Requirements and test procedures for aerodynamics on open track," CEN EN 14067–4 (2013).
[44]Z.-X. Che, Z.-W. Chen, Y.-Q. Ni, S. Huang, and Z.-W. Li, "Research on the impact of air-blowing on aerodynamic drag reduction and wake characteristics of a high-speed maglev train," Phys. Fluids **35**, 115138 (2023).
[45]J. Zhang, A. Xu, F. Huang, Y. Bai, and T. Liu, "A novel vortex control method for improving anti-overturning performance of a high-speed train with leeward airbag structures under crosswinds," Phys. Fluids **36**(6), 065146 (2024).
[46]J. Zhang, Y. Ding, F. Wang, N. Xiang, A. Xu, Z. Chen, and M. Tang, "Comparison of aerodynamic performance of trains running on bridges under crosswinds using various motion modes," Phys. Fluids **35**(12), 125125 (2023).
[47]Z.-W. Chen, Z.-J. Guo, Z.-X. Che, Z.-D. Huang, Y.-Q. Ni, S.-M. Wang, S. Huang, Z.-W. Li, and Q.-X. Wang, "Evaluation of active leeward side air-blowing layout on the lateral aerodynamic performance of high-speed trains in crosswinds environment: Sustainable and safe operation strategy," J. Wind Eng. Ind Aerodyn. **247**, 105695 (2024).
[48]S. Han, F. Wang, and J. Zhang, "Influence of inflow conditions on simplified heavy vehicle wake," Phys. Fluids **36**(4), 045151 (2024).
[49]D. Zhang, Z.-H. Guo, Y.-Q. Ni, Z.-W. Chen, W. K. Ao, A. Bordbar, and F.-R. Zhou, "Correlation between cargo properties and train overturning safety for a high-speed freight train under strong winds," Eng. Appl. Comput. Fluid Mech. **17**, 2221308 (2023).

09 January 2026 03:26:12

Published under an exclusive license by AIP Publishing

[50]W. Shi, J. Li, H. Gao, H. Zhang, Z. Yang, and Y. Jiang, "Numerical investigations on drag reduction of a civil light helicopter fuselage," Aerosp. Sci. Technol. **106**, 106104 (2020).
[51]C. Tan, D. Zhou, G. Chen, J. Sheridan, and S. Krajnovic, "Influences of marshalling length on the flow structure of a maglev train," Int. J. Heat Fluid Flow **85**, 108604 (2020).
[52]Z.-D. Huang, Z.-B. Zhou, N. Chang, Z.-W. Chen, and S.-M. Wang, "Aerodynamic features of high-speed maglev trains with different marshaling lengths running on a viaduct under crosswinds," CMES **140**, 975 (2024).
[53]F. Alff, U. Brummund, W. Clauss, M. Oschwald, J. Sender, and W. Waidmann, "Experimental investigation of the combustion process in a supersonic combustion ramjet (SCRAMJET) combustion chamber," (DLR, 1994).
[54]R. Hönig, D. Theisen, R. Fink, R. Lachner, G. Kappler, D. Rist, and P. Andresen, "Experimental investigation of a SCRAMJET model combustor with injection through a swept ramp using laser-induced fluorescence with tunable excimer lasers," in *Symposium (International) on Combustion* (Elsevier, 1996), Vol. 26, p. 2949.
[55]M. V. Silnikov, M. V. Chernyshov, and V. N. Uskov, "Analytical solutions for Prandtl–Meyer wave–oblique shock overtaking interaction," Acta Astronaut. **99**, 175 (2014).
[56]K. Ananthakrishnan and M. Govardhan, "Influence of fillet shapes on secondary flow field in a transonic axial flow turbine stage," Aerosp. Sci. Technol. **82–83**, 425 (2018).
[57]M. Dharavath, P. Manna, and D. Chakraborty, "Thermochemical exploration of hydrogen combustion in generic scramjet combustor," Aerosp. Sci. Technol. **24**, 264 (2013).
[58]J. Panda and R. G. Seasholtz, "Measurement of shock structure and shock–vortex interaction in underexpanded jets using Rayleigh scattering," Phys. Fluids **11**, 3761 (1999).

09 January 2026 03:26:12

Published under an exclusive license by AIP Publishing